

The WAGGS project - III. Discrepant mass-to-light ratios of Galactic globular clusters at high metallicity

H. Dalglish¹★, S. Kamann¹, C. Usher¹, H. Baumgardt², N. Bastian¹,
J. Veitch-Michaelis¹, A. Bellini³, S. Martocchia^{4,1}, G. S. Da Costa⁵,
D. Mackey⁵, S. Bellstedt⁶, N. Pastorello⁷, P. Cerulo⁸

¹*Astrophysics Research Institute, Liverpool John Moores University, Liverpool, L3 5RF, UK*

²*School of Mathematics and Physics, The University of Queensland, St. Lucia, QLD 4072, Australia*

³*Space Telescope Science Institute, 3800 San Martin Drive, Baltimore, MD 21218, USA*

⁴*European Southern Observatory, Karl-Schwarzschild-Strasse 2, D-85748, Garching bei München*

⁵*Research School of Astronomy and Astrophysics, Australian National University, Canberra, ACT 2611, Australia*

⁶*ICRAR, The University of Western Australia, 7 Fairway, Crawley WA 6009, Australia*

⁷*BlueScope, Level 11, 120 Collins Street, Melbourne VIC 3000, Australia*

⁸*Department of Astronomy, Universidad de Concepción, Casilla 160-C, Concepción, Chile*

Accepted XXX. Received YYY; in original form ZZZ

ABSTRACT

Observed mass-to-light ratios (M/L) of metal-rich globular clusters (GCs) disagree with theoretical predictions. This discrepancy is of fundamental importance since stellar population models provide the stellar masses that underpin most of extragalactic astronomy, near and far. We have derived radial velocities for 1,622 stars located in the centres of 59 Milky Way GCs — twelve of which have no previous kinematic information — using integral-field unit data from the WAGGS project. Using N -body models, we determine dynamical masses and M/L_V ratios for the studied clusters. Our sample includes NGC 6528 and NGC 6553, which extend the metallicity range of GCs with measured M/L up to $[\text{Fe}/\text{H}] \sim -0.1$ dex. We find that metal-rich clusters have M/L_V more than 2 times lower than what is predicted by simple stellar population models. This confirms that the discrepant M/L – $[\text{Fe}/\text{H}]$ relation remains a serious concern. We explore how our findings relate to previous observations, and the potential causes for the divergence, which we conclude is most likely due to dynamical effects.

Key words: globular clusters: kinematics and dynamics

1 INTRODUCTION

Globular clusters (GCs) contain large numbers ($10^5 - 10^6$) of stars of roughly the same age and metallicity. For this reason, GCs are ideal laboratories for the study of the formation and evolution of stars and their host galaxies (e.g. Ashman & Zepf 1998). In particular, internal cluster kinematics have a key role in our understanding of GCs and their origins.

When research on this topic began in the late 1970s, studies depended on limited radial velocity information to derive velocity dispersions, dynamical masses, and other important cluster parameters (Pryor & Meylan 1993, and references therein). King (1966) models — and variations thereof — have commonly been used for this work, however static models such as these suffer limitations; they cannot account for cluster relaxation, a result of gravitational interactions

of their member stars. Therefore, phenomena such as mass segregation, mass loss, or core collapse cannot be understood using these one-component static models. Multi-component static models, on the other hand, can take such evolutionary dynamical processes into account (see e.g. Tornamenti et al. 2019). They can be analytical, like the isotropic multi-mass King-Michie models (Gunn & Griffin 1979), LIMEPY models (Gieles & Zocchi 2015), N -body models (Zonoozi et al. 2011; Heggie 2014; Wang et al. 2016; Baumgardt 2017; Baumgardt & Hilker 2018), or Monte-Carlo models. Most recently, Baumgardt et al. (2019a) have used N -body models to determine masses, structural parameters, and mass-to-light ratios of 144 GCs, where they also included *Gaia* DR2 proper motions besides radial velocities.

The available kinematic data are often a significant limitation when constraining cluster parameters via evolutionary models. *Gaia* and most ground-based multi-object spectrographs like VLT/FLAMES or Keck/DEIMOS are unable

★ E-mail: h.s.dalglish@2016.ljmu.ac.uk

to observe a large number of stars within the core radii of GCs because of the strong stellar crowding in those regions. Given the short relaxation times and expected overdensities of stellar remnants near the centres (due to mass segregation), it is likely a key area of parameter space has been missed. Now with *HST* and the development of integral-field units (IFUs) like MUSE, studies can measure the motions of thousands of stars — including those in the cluster centres — for the first time (e.g. Bellini et al. 2014, 2017b; Kamann et al. 2018; Ferraro et al. 2018). This has opened up new avenues to uncover the populations of central stellar remnants, like stellar-mass black holes (e.g. Giesers et al. 2018, 2019; Baumgardt et al. 2019b), which can further aid our understanding of the internal structures of GCs.

One puzzle yet to be solved is the notable discrepancy between theoretical predictions and observations of GC M/L ratios. Simple stellar population (SSP) models predict that the mass-to-light ratio in the V band (M/L_V) should increase with metallicity — given a constant initial mass function (IMF) — as a result of line blanketing (e.g. Bruzual & Charlot 2003; Maraston 2005; Conroy & Gunn 2010). However, Djorgovski et al. (1997) and Strader et al. (2009, 2011) found that for the globular clusters in M31, M/L decreases with $[\text{Fe}/\text{H}]$. In the Milky Way, the situation appears to be similar; Kimmig et al. (2015) showed that M/L is $\gtrsim 2$ times lower than expected for clusters at the metal-rich end. Equally, Baumgardt (2017) found that the observed M/L - $[\text{Fe}/\text{H}]$ relation also disagrees with SSP models: they find no change of M/L with cluster metallicity. Very few metal-rich Galactic clusters ($[\text{Fe}/\text{H}] > -0.5$ dex) were included in the studies of Kimmig et al. (2015) and Baumgardt (2017), however, so it is unclear if the discrepancy for MW clusters is as pronounced as it is for M31 towards solar metallicity. This is further emphasised by Shanahan & Gieles (2015), who discuss the challenges of reliably measuring the M/L of star clusters from integrated light.

Understanding where the discrepancy between observed M/L and SSP model predictions originates is key. SSP models are used to determine a wide range of important properties — including stellar masses, star formation histories and metallicities — from the integrated light of galaxies and extragalactic star clusters (e.g. Gallazzi & Bell 2009; Conroy 2013; Martins et al. 2019). Furthermore, the mismatch between observed stellar M/L and SSP model predictions has been used to constrain the IMF (e.g. Cappellari et al. 2012; Newman et al. 2013). Hence, more high-resolution observations of metal-rich clusters are needed to confirm the discrepancy between theory and observation.

WAGGS, the WiFeS Atlas of Galactic Globular cluster Spectra survey (Usher et al. 2017, 2019) has already significantly extended GC observations to include younger and more metal-rich clusters. The survey is also particularly advantageous since it covers the central regions of all clusters ($\lesssim 20$ arcsec). Our study uses the WAGGS survey to fill this gap in the literature, with newly-determined central velocity dispersions, dynamical masses, and M/L_V for 59 globular clusters in the Milky Way. For twelve of these GCs, M/L_V have never before been derived, due to the lack of kinematic information.

We organise the paper as follows: our observations are described in Section 2, followed by a description of our data reduction and analysis (Section 3). The results and discus-

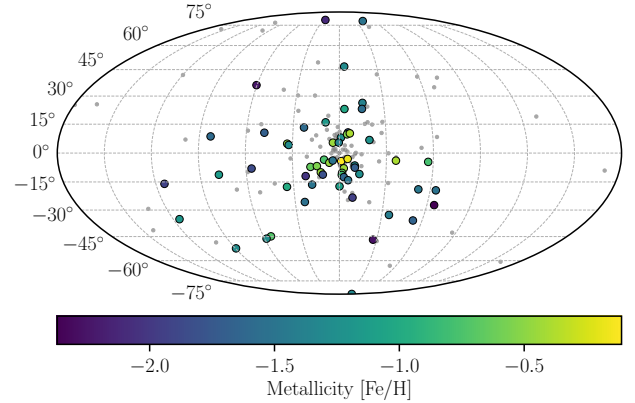


Figure 1. Milky Way globular clusters projected in Mollweide space in Galactic coordinates. The subset of 59 globular clusters from the WAGGS survey used in this study are highlighted: the most metal-rich clusters appear yellow and are found towards the bulge, and the most metal-poor clusters are in purple, typically found towards the halo. Any remaining Milky Way GCs are shown as grey dots (Harris 1996, 2010).

sion are presented in Sections 4 and 5 respectively, with concluding remarks made in Section 6.

2 OBSERVATIONS

For this work, we studied a subset of 59 GCs taken from the WAGGS survey (Figure 1). The clusters were selected on the basis that they either have *HST* photometry and imaging publicly available, they are metal-rich (i.e. NGCs 6528 and 6553), or there are fewer than 25 radial velocity measurements in the Baumgardt et al. (2019a) sample.

WAGGS observations were made between 2015 and 2018 using WiFeS, the Wide-Field Spectrograph, on the 2.3-m ANU telescope (Dopita et al. 2007, 2010). WiFeS is an IFU spectrograph with a field-of-view of 38×25 arcsec. We used the four higher resolution gratings (U7000, B7000, R7000, and I7000) in two setups to cover the wavelength range 3300–9000 Å with spectral resolution, $R \sim 6800$. Further details regarding the observations and data reduction can be found in Usher et al. (2017). In addition to the observations described in Usher et al. (2017, 2019), we include new observations of NGCs 6325, 6355, 6380, 6453, 6528, 6553, and 6760 carried out between September 10th–13th 2018. Of these, NGC 6528 and NGC 6553 had already been observed before. Unlike most WAGGS observations, where only a single pointing centred on the GC centre was observed, for the new NGC 6528 and NGC 6553 observations we tiled the centres of these GCs with four pointings. We reduced the September 2018 observations using PyWiFeS (Childress et al. 2014b,a) in the same manner as described in Usher et al. (2017).

2.1 Photometry

Photometry for the clusters is required to extract the spectra from the WAGGS datacubes (see Section 3.1) and comes from previous literature wherever possible. For the majority of GCs, we obtained existing *HST* photometry from the UV

Table 1. List of newly analysed *HST* observations used for this project.

Cluster	Camera	Filter	Exposures	Program ID	Epoch
NGC 5946	WFC3/UVIS	F438W	3×500 s	11628	2009.6
		F555W	3×80 s		
NGC 6325	WFC3/UVIS	F438W	3×435 s	11628	2010.3
		F555W	3×85 s		
NGC 6342	WFC3/UVIS	F438W	3×420 s	11628	2009.6
		F555W	3×80 s		
NGC 6355	WFC3/UVIS	F438W	3×440 s	11628	2009.6
		F555W	3×80 s		
NGC 6380	WFC3/UVIS	F555W	3×440 s	11628	2010.2
		F814W	3×80 s		
NGC 6453	WFC3/UVIS	F438W	3×450 s	11628	2010.4
		F555W	3×80 s		
NGC 6517	WFC3/UVIS	F555W	3×420 s	11628	2010.3
		F814W	3×100 s		
NGC 6553	ACS/WFC	F435W	3×340 s	10753	2006.3
		F555W	1×300 s		
		F814W	1×60 s		

Legacy Survey (Soto et al. 2017). NGC 6528 photometry was sourced from the Hubble Legacy Archive, in programs 5436 (PI: Ortolani), 8696 (PI: Feltzing), 9453 (PI: Brown), 11664 (PI: Brown), and the photometry for NGC 6356 and NGC 7006 were obtained from Piotto et al. (2002) and Dotter et al. (2011), respectively. For eight of the clusters, photometry was not available (i.e. NGCs 5946, 6325, 6342, 6355, 6380, 6453, 6517, and 6553). These remaining clusters were reduced using *HST* observations as shown in Table 1.

The reduction of all *HST* exposures is based on `_flc` images. These images have been corrected for the flat-field and charge-transfer efficiency effects (Anderson & Bedin 2010; Anderson & Ryon 2018) and bias-subtracted via the standard *HST* pipelines, and contain the unresampled pixel data for stellar-profile fitting.

2.1.1 NGCs 5946, 6325, 6342, 6355, 6380, 6453, 6517

The data for the first seven clusters are obtained from GO-11628 (P.I.: E. Noyola) and we measured the stellar photometry as follows. First, for each exposure, we derived state-of-the-art, spatially variable PSF models by perturbing the library PSF models created by Jay Anderson¹ in order to account for telescope breathing effects (di Nino et al. 2008, see also Bellini et al. 2017a, 2018a). Using these PSFs, we measure stellar positions and fluxes of bright sources in each exposure (including saturated stars) using the FORTRAN code `HST1pass` (Anderson in prep., see Bellini et al. 2018b for details). Photometry of the saturated stars is obtained by including all the relevant flux from the bled-into pixels following the prescriptions given in Gilliland et al. (2010). This technique allows us to achieve 5% photometric RMS three magnitudes above saturation. Stellar positions and magnitudes in these single-exposure catalogues are corrected for geometric distortion and pixel-area (Bellini et al. 2011).

We used the *Gaia* DR2 catalogue (Gaia Collaboration et al. 2016, 2018) to define a reference frame with a pixel scale of exactly 50 mas. We transformed stellar positions from each single-exposure catalogue on to the reference frame by means of six-parameter linear transformations using bright, unsaturated stars.

Next, we obtain best estimates of positions and fluxes for all possible sources, using the FORTRAN software package `KS2` (Anderson, in prep., see Bellini et al. 2017a for details). `KS2` takes the image-tailored PSF models and six-parameter linear transformations of each catalogue on to the reference frame, and uses all the exposures simultaneously to find, measure and subtract sources through different finding waves. `KS2` measures stellar photometry using three different methods, each of which is best suited for specific brightness regimes. Since our primary objective is to derive reliable mass-to-light ratios, we relied on `KS2`’s “method 1”, which offers the best photometry for intermediate and high brightness regimes.

2.1.2 NGC 6553

The NGC 6553 photometric catalogue is obtained from GO-10573 (P.I.: M. Mateo). We corrected for pixel-area effects by applying Pixel Area Maps to each `_flc` image as well as cosmic ray contamination by using the L.A. Cosmic algorithm (van Dokkum 2001). We followed the same strategy as Dalessandro et al. (2014) for the photometric analysis:

First we used DAOPHOTIV (Stetson 1987) independently on each chip and filter. Several hundreds of bright and isolated stars were selected in order to model the PSF. All available analytic functions were considered for the PSF fitting (i.e. Gauss, Moffat, Lorentz and Penny functions), leaving the PSF free to spatially vary to the first-order. For each image, we fit all the star-like sources with the obtained PSF using a threshold of 3σ from the local background. Next, we used ALLFRAME (Stetson 1984) to generate a star list with stars detected in at least three out of the five

¹ www.stsci.edu/~jayander/WFC3/

images, when putting all the filters together, one chip at a time. The final star lists for each image and chip were cross-correlated using DAOMATCH, followed by magnitude means and standard deviations with DAOMASTER. We obtained the final catalogue through matching the star lists for each filter via DAOMATCH and DAOMASTER. Finally, instrumental magnitudes were converted to the VEGAMAG photometric system given the prescriptions and zero-points reported on the ACS webpage² and in Sirianni et al. (2005).

3 DATA REDUCTION AND ANALYSIS

3.1 Stellar spectra

In order to extract the stellar spectra from the WAGGS data cubes, we used PAMPELMUSE (Kamann et al. 2013). The software optimally extracts the spectrum of each resolved star from a cube using an analytical model of the point-spread function (PSF). The model parameters can be wavelength-dependent and are optimized during the fit. The coordinates of each resolved source are inferred from the source catalogs described in Sect. 2.1. The PSF-fitting technique allows one to de-blend clean stellar spectra even in crowded stellar fields such as the centres of GCs.

As our analysis aims to maximize the number of extracted stars, it will always yield a fraction of spectra with a signal-to-noise (S/N) that is not high enough ($\gtrsim 5 \text{ \AA}^{-1}$) for a meaningful analysis. This problem often affected the spectra of red giant branch stars observed with the U7000 and B7000 gratings, in particular for clusters with high extinctions. Example spectra of an asymptotic giant branch star from NGC 6752 (*Gaia* DR2 ID: 6632372787224214912) can be seen in Figure 2. The S/N per pixel is higher than the typical observed spectra, and is as follows: 14.3 (U7000), 24.4 (B7000), 26.1 (R7000), and 29.6 (I7000).

For each spectrum, effective temperature (T) and surface gravity ($\log g$) were determined by over-plotting MIST (MESA Isochrones & Stellar Tracks) isochrones (Dotter 2016; Choi et al. 2016; Paxton et al. 2011, 2013, 2015) on a colour-magnitude diagram (CMD). We assumed an age of 12.59 Gyr for each cluster and adopted the metallicities in the 2010 edition of the Harris (1996, 2010) catalogue. An example $m_{F606W} - m_{F814W}$ versus m_{F606W} CMD for NGC 6752 can be seen in Figure 3. The stellar spectra were cross-correlated against a grid of T and $\log g$ values corresponding to a synthetic PHOENIX template spectrum (Husser et al. 2013). GC α -element abundances (either $[\alpha/\text{Fe}] = 0.2$ or 0.4) were, in the first instance, taken from Carretta et al. (2010). In the second instance, we used Dias et al. (2016) in the absence of Carretta et al. (2010) data. For the clusters lacking $[\alpha/\text{Fe}]$ measurements, $[\alpha/\text{Fe}] = 0.4$ was used.

We determined radial velocities using FXCOR in PyRAF (Greenfield & White 2000, 2006; de La Peña et al. 2001; Science Software Branch at STScI 2012); a task based on the Fourier cross-correlation method developed by Tonry & Davis (1979). The wavelength ranges used for the cross-correlation were selected in order to include important lines (e.g. Calcium triplet, H α) while avoiding telluric lines. We used wavelength ranges as follows: I7000 grating ($\lambda\lambda = 8450$ –

8700 \AA); R7000 grating ($\lambda\lambda = 6400$ – 6800 \AA); B7000 grating ($\lambda\lambda = 4800$ – 5200 \AA); and U7000 grating ($\lambda\lambda = 3800$ – 4200 \AA), shown by the grey dashed lines in Figure 2. Since each spectrum was cross-correlated against a grid of PHOENIX spectra, the radial velocity with the highest Tonry and Davis Ratio (TDR ; a measure of how good the fit is) was used.

Similar to the method of Kamann et al. (2014), we plot systemic velocities from each grating against S/N in log-log space (Figure 4), in order to remove unreliable measurements from the RV sample. $S/N > 8$ and $TDR > 13$ yielded 4136 stars for all 59 clusters, whereas $S/N > 7$ and $TDR > 16$ yielded 4258 stars, thus we chose the latter in order to retain the largest number of stars. The grey dotted line in Figure 4 depicts the cut at $S/N = 7$, and spectra shown as small dots have values of $TDR < 16$. The same cut was used for all four gratings. After applying these cuts we are left with a sample of 29, 631, 1169, and 2429 spectra in the U7000, B7000, R7000, and I7000 gratings, respectively.

To account for nightly systematic variances between the different gratings, we calculated a shift in velocity between the different gratings, relative to the I7000 grating, per star per night. The I7000 grating was chosen since it contains the greatest number of spectra with the smallest uncertainties. Averaging the shifts for all stars each night, we applied a correction to the radial velocities in the U7000, B7000, and R7000 gratings (Figure 5).

After averaging the velocities obtained from the different gratings, we applied sigma clipping ($\sigma = 3$) to exclude any outliers in velocity space. For NGC 6496, for which we have very few stars, two clear outliers were still present (with radial velocities differing by $\sim 160 \text{ km/s}$), and were removed by hand. Overall, we use only sufficiently accurate velocity measurements, usually velocity errors less than 1.5 – 2 km/s , depending on the internal velocity dispersion of the cluster.

3.2 N -body models

We compared the observational data of each globular cluster with a large grid of 2,500 N -body simulations. To this end, we ran N -body simulations of isolated star clusters — each containing $N = 100,000$ stars — using the GPU-enabled version of the collisional N -body code NBODY6 (Nitadori & Aarseth 2012). The simulated clusters followed King (1962) density profiles with variations of initial concentrations ($0.2 \leq c \leq 2.5$) and initial radii ($2 \leq r_h \leq 35 \text{ pc}$). We also varied the initial mass function of the star clusters from those following an initial Kroupa (2001) mass function to clusters highly depleted in low-mass stars.

All simulations were run up to an age of $T = 13.5 \text{ Gyr}$ and final cluster models were calculated by taking 10 snapshots from the simulations centred around the age of each GC. The combined snapshots of the N -body clusters were scaled in mass and radius to match the density and velocity dispersion profiles of the observed globular clusters and the best-fitting model was determined by interpolating in the grid of N -body simulations. Further details of the performed N -body simulations can be found in Baumgardt (2017) and Baumgardt & Hilker (2018).

² <http://acszeropoints.stsci.edu/>

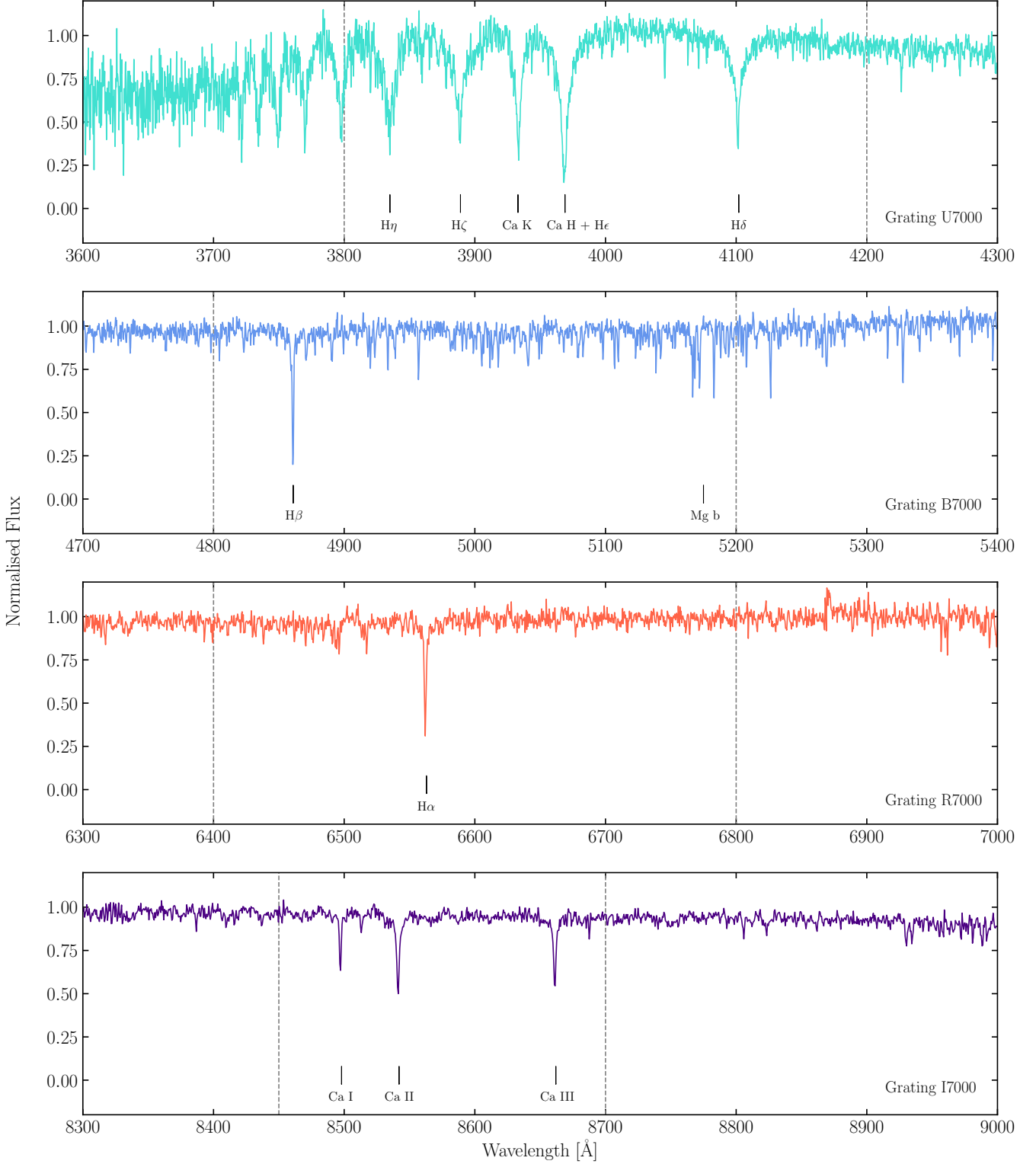


Figure 2. Example spectra (*Gaia* DR2 ID: 6632372787224214912) of an asymptotic giant branch star in NGC 6752 extracted by PampelMuse across four different gratings (U7000, turquoise; B7000, blue; R7000, red; I7000, purple). The grey dashed lines mark the wavelength ranges used to cross-correlate against the PHOENIX template spectra. The wavelength ranges were chosen to avoid telluric lines. Prominent hydrogen and calcium lines are also marked.

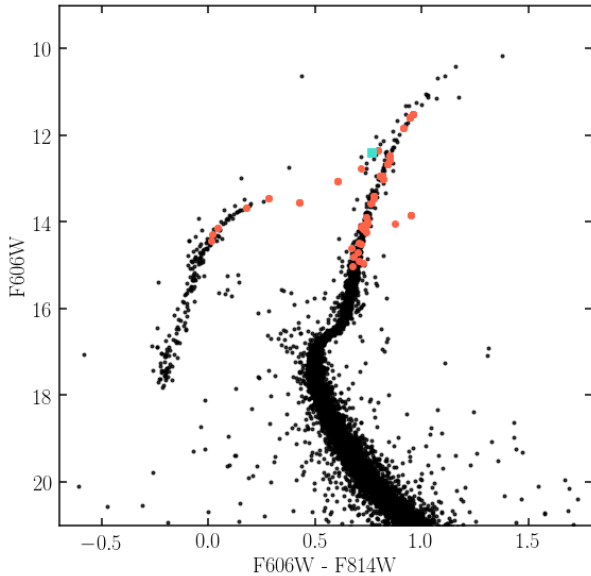


Figure 3. An example colour-magnitude diagram of NGC 6752 with photometry from the UV Legacy Survey (Soto et al. 2017). Stars with WAGGS spectra are marked in red. The turquoise square corresponds to the spectrum depicted in Figure 2.

4 RESULTS

We combine the WAGGS radial velocities with the Baumgardt et al. (2019a) data and fit the N -body models to each cluster. Each set of velocity measurements are shifted to a common velocity by cross-matching the different data sets against each other to correct for zero-point offsets. We then cross-correlate against *Gaia* position measurements to get proper motion information in order to select which stars to use, replacing any original positions with the *Gaia* positions if a match is found. We finally average all velocity measurements for each star and exclude any stars with varying radial velocities.

For the WAGGS data there is the added complication that the stars are located in the crowded cluster centres where *Gaia* measurements are lacking, and all data come with position errors. About 20-100% of the WAGGS stars have *Gaia* counterparts depending on completeness. We use a small search radius (0.5") to minimise erroneous cross identifications.

In the end, we increase the Baumgardt et al. (2019a) dataset with 1,622 WAGGS measurements, within approximately 20 arcsec from the cluster centres (Figure 6). This is smaller than the half-light radii, where the ratio of observed to half-light radius is ~ 0.3 on average, and ranges between 0.1 (for the more dispersed) and 0.8 (for the more compact GCs). The dataset can be found online³. For 16 of the clusters, the number of velocity measurements has increased by more than 50%.

Velocity dispersion profiles are determined by combining the velocity measurements with *Gaia* proper motions (where available). The stars are ordered according to central distance before calculating velocity dispersion (using a

maximum likelihood approach, see Pryor & Meylan 1993) and χ^2 for each member — those with too large χ^2 are removed. This process is repeated until a stable solution is found. Velocity errors have been taken into account.

We then combine each velocity dispersion profile with the corresponding surface density profile and stellar mass function in order to derive cluster mass. This is done by fitting a grid of N -body simulations to the combined data as described in Baumgardt (2017); Baumgardt & Hilker (2018) — examples of which can be seen in Figure 7.

Cluster M/L_V ratios are calculated by taking the mean cluster luminosity from Harris (1996); McLaughlin & van der Marel (2005); Dalessandro et al. (2012) in addition to luminosity determinations from Baumgardt & Hilker (2018). The results are presented in Table 2.

4.1 Comparisons to Previous Work

We compare our derived velocity dispersions and masses with previous work: 20 clusters overlap with the Kimmig et al. (2015) sample; and ten can be compared to Ferraro et al. (2018). The central velocity dispersions derived by each study are (King) model predictions based on velocity dispersions further out. For completeness, we also compare the results of Baumgardt et al. (2019a) to ours. Twelve clusters (NGCs 5946, 6325, 6333, 6342, 6355, 6356, 6380, 6453, 6517, 6642, 6760, 7006) are previously little studied, and thus cannot be compared.

Figure 8 shows our central velocity dispersions compared to the aforementioned literature. The most significant discrepancies lie with the results of Kimmig et al. (2015), particularly for NGCs 2808, 6715, and 7078. We further observe a trend for the central velocity dispersions of Ferraro et al. (2018) to be lower than ours. As their results are based on multi-object spectroscopy, this could be caused by differences in the average distances of the sample stars to the cluster centres. Also, contamination from nearby sources or the unresolved cluster light can be an issue near the centres. However, as our analysis explicitly accounts for these effects, we are confident that our values are robust against such contamination.

Figure 9 shows our derived cluster masses compared to Kimmig et al. (2015); Ferraro et al. (2018); Baumgardt et al. (2019a). As before, three of the Kimmig et al. (2015) cluster values are the most discrepant, although for different GCs: NGCs 288, 6809, and 6838. The majority of the Ferraro et al. (2018) masses are shifted towards lower masses, which appears to be a consequence of the on-average lower dispersion measurements in the study of Ferraro et al. (2018).

5 THE MASS-TO-LIGHT RATIO

The M/L depends on the proportion of high- to low-mass stars within a cluster. Massive stars contribute most of the light within a cluster, whereas the low-mass stars and stellar remnants (white dwarfs, neutron stars and black holes) contribute most of the mass. As such, the M/L provides an important insight into stellar evolution and the stellar mass function, and is a very useful tool for checking and constraining SSP models.

We plot the M/L_V -[Fe/H] relation of 59 Milky Way

³ <https://people.smp.uq.edu.au/HolgerBaumgardt/globular/>

Table 2. Derived structural parameters for the 59 Milky Way globular clusters considered in this work. From left to right we list the GC name; metallicity (Harris 1996, 2010); mass and associated error; mass-to-light ratio and error; (1D) central velocity dispersion; total number of stars; and total number of WAGGS stars in the sample. Additional parameter values can be found at <https://people.smp.uq.edu.au/HolgerBaumgardt/globular/>

GC Name	[Fe/H] dex	Mass $\times 10^5 M_\odot$	Δ Mass	M/L _V M_\odot/L_\odot	Δ M/L _V	σ_0 km/s	N _{total}	N _{WAGGS}
NGC 104	-0.72	8.07	0.05	1.82	0.17	12.3	3254	78
NGC 288	-1.38	1.21	0.03	2.39	0.17	3.3	528	1
NGC 362	-1.26	3.37	0.05	1.7	0.25	8.9	479	19
NGC 1261	-1.27	1.73	0.15	2.2	0.38	5.6	288	39
NGC 1851	-1.18	2.83	0.04	1.92	0.14	10.6	669	58
NGC 2298	-1.92	0.54	0.1	2.11	0.42	3.5	40	8
NGC 2808	-1.14	8.18	0.06	1.67	0.12	15.0	1135	88
NGC 3201	-1.59	1.46	0.05	2.46	0.42	4.4	721	14
NGC 4590	-2.23	1.29	0.11	2.33	0.46	3.9	248	11
NGC 4833	-1.85	2.03	0.12	1.29	0.25	4.9	162	17
NGC 5024	-2.10	4.28	0.35	1.79	0.21	6.2	334	21
NGC 5272	-1.50	3.61	0.16	1.57	0.22	8.0	668	24
NGC 5286	-1.69	3.79	0.17	1.39	0.13	9.4	523	37
NGC 5904	-1.29	3.66	0.06	1.47	0.19	7.8	827	36
NGC 5927	-0.49	3.44	0.03	2.17	0.3	7.1	395	60
NGC 5946	-1.29	0.75	0.20	1.17	0.35	5.5	33	24
NGC 5986	-1.59	3.31	0.24	1.95	0.27	8.2	237	15
NGC 6121	-1.16	0.90	0.02	1.96	0.11	4.7	2817	11
NGC 6171	-1.02	0.77	0.04	2.19	0.61	4.1	373	22
NGC 6218	-1.37	0.82	0.04	1.51	0.34	5.0	495	13
NGC 6254	-1.56	1.88	0.04	1.8	0.06	6.2	406	16
NGC 6304	-0.45	1.61	0.14	2.12	0.38	5.3	171	5
NGC 6325	-1.25	0.73	0.12	1.65	0.45	6.3	42	34
NGC 6333	-1.77	3.16	0.24	2.28	0.22	8.2	34	25
NGC 6342	-0.55	0.60	0.11	3.64	1.52	5.6	49	33
NGC 6352	-0.64	0.55	0.02	1.79	0.17	3.3	40	8
NGC 6355	-1.37	0.71	0.14	0.57	0.15	5.2	50	32
NGC 6356	-0.40	3.82	0.80	1.55	0.36	7.6	44	23
NGC 6362	-0.99	1.08	0.03	2.25	0.12	3.6	342	3
NGC 6380	-0.75	3.05	0.02	2.06	2.73	8.1	46	36
NGC 6388	-0.55	10.4	0.09	1.87	0.23	17.7	511	26
NGC 6397	-2.02	0.89	0.01	2.23	0.35	5.4	2399	11
NGC 6441	-0.46	11.7	0.11	2.01	0.13	18.9	214	10
NGC 6453	-1.50	2.33	0.02	3.54	0.99	7.7	21	19
NGC 6496	-0.46	0.84	0.12	1.84	1.08	3.3	127	7
NGC 6517	-1.23	3.04	0.55	2.18	0.71	11.5	32	16
NGC 6528	-0.11	0.60	0.07	1.5	0.43	5.0	159	117
NGC 6541	-1.81	2.50	0.08	1.52	0.53	8.7	206	49
NGC 6553	-0.18	3.01	0.16	2.12	0.28	7.9	499	138
NGC 6584	-1.50	1.16	0.02	1.43	0.35	4.1	26	20
NGC 6624	-0.44	0.62	0.02	0.99	0.12	5.9	344	6
NGC 6637	-0.64	1.48	0.16	0.84	0.16	6.4	62	48
NGC 6642	-1.26	0.25	0.07	0.71	0.2	4.1	20	13
NGC 6652	-0.81	0.46	0.08	1.48	0.42	5.1	40	37
NGC 6656	-1.70	4.05	0.04	1.93	0.07	8.6	800	19
NGC 6681	-1.62	1.13	0.02	1.95	0.27	7.1	52	21
NGC 6715	-1.49	15.9	0.19	2.18	0.1	16.9	533	16
NGC 6717	-1.26	0.36	0.08	2.09	0.58	3.2	17	14
NGC 6723	-1.10	1.73	0.11	1.89	0.29	5.5	368	20
NGC 6752	-1.54	2.30	0.03	2.15	0.34	8.3	1184	37
NGC 6760	-0.40	2.57	0.30	2.01	0.27	7.2	80	53
NGC 6809	-1.94	1.87	0.07	2.79	0.55	4.9	492	18
NGC 6838	-0.78	0.53	0.03	2.8	1.04	2.9	256	14
NGC 6934	-1.47	1.40	0.25	1.73	0.31	4.9	45	12
NGC 6981	-1.42	0.68	0.12	1.22	0.23	3.0	21	19
NGC 7006	-1.52	1.47	0.38	1.94	0.52	4.0	43	18
NGC 7078	-2.37	4.94	0.05	1.18	0.11	13.6	1273	6
NGC 7089	-1.65	5.05	0.10	1.68	0.06	10.7	410	21
NGC 7099	-2.27	1.27	0.07	1.8	0.38	5.5	709	6

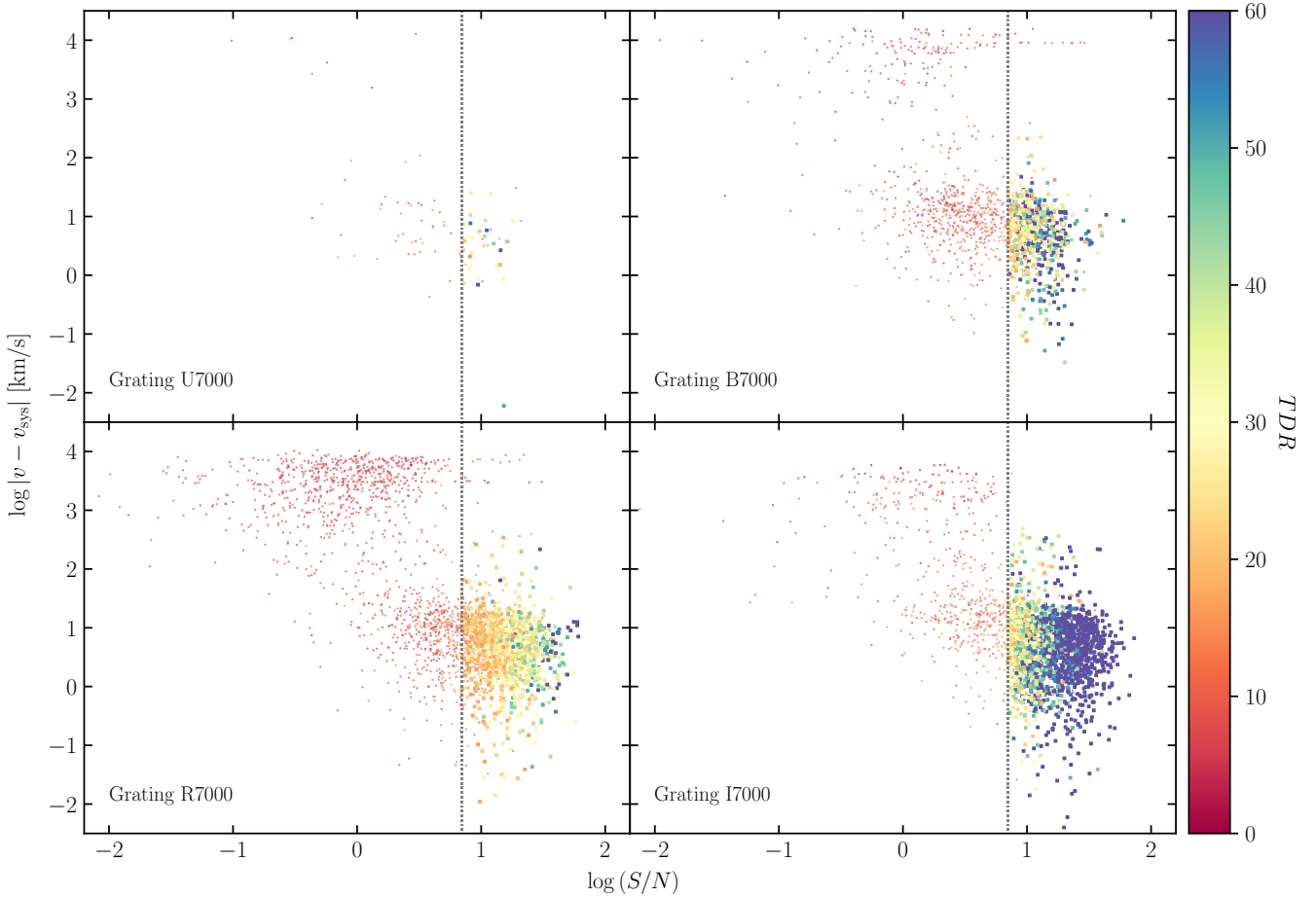


Figure 4. Absolute velocity difference (with respect to the cluster systemic velocity) versus S/N for all spectra for each grating in log-log space. The spectra belong to all 59 clusters and are coloured according to their TDR value. Spectra with $TDR < 16$ (shown as small dots) and $S/N < 7$ (grey dotted lines) are deemed unreliable and have been excluded from further analysis. A maximum of $TDR = 60$ has been applied to better see the spectra at lower values.

globular clusters, reaching higher metallicities — $[\text{Fe}/\text{H}] > -0.4$ dex — than seen before (Figure 10). The median M/L_V is shown as a grey dashed line ($1.9 M_\odot/L_\odot$). We find no trend with $[\text{Fe}/\text{H}]$, with Spearman’s rank correlation coefficient, $\rho = -0.01$. However, even after accounting for observational errors, a cluster-to-cluster scatter is clearly visible. In particular, we note five outliers:

- (i) NGCs 6342 and 6453 ($M/L_V \sim 3.6 M_\odot/L_\odot$) both have large uncertainties, which can be explained by uncertain total cluster luminosities. Newly derived luminosities (Baumgardt, in prep) decrease the M/L_V of these clusters.
- (ii) NGCs 6355, 6637, and 6642 have low dynamical M/L_V ($< 0.9 M_\odot/L_\odot$) and small uncertainties, also likely due to unreliable luminosities and underestimated errors. Baumgardt (in prep) finds more reliable luminosities, which lead to $M/L_V > 1$ for all four clusters. Determining accurate luminosities is difficult due to close proximity to the bulge of all three clusters (in galactocentric radius, $1.0 < R_{GC} < 1.7$ kpc).

In addition to the above, measuring M/L itself is known to be model-dependent, often with a scatter of 20% or more (e.g. Zocchi et al. 2017, Table 2, and Bellini et al. 2017b, Ta-

ble 8). However, such errors should not correlate with metallicity; while our errors do not take into account systematic errors introduced by the N -body models, it is unlikely that they will counterbalance systemic offsets at high metallicity.

We compare our observations with theoretical predictions by over-plotting stellar population models (Figure 10; blue line). The models are calculated using version 3.0 of the Flexible Stellar Population Synthesis (FSPS) code (Conroy et al. 2009; Conroy & Gunn 2010), MIST isochrones (Dotter 2016; Choi et al. 2016; Paxton et al. 2011, 2013, 2015), a Kroupa (2001) IMF and the MILES spectral library (Sánchez-Blázquez et al. 2006). We also tested the UV-extended E-MILES stellar population models from Vazdekis et al. (2016), using both the BaSTI (Pietrinferni et al. 2004) and Padova (Girardi et al. 2000) theoretical isochrones. We find good agreement between all predicted M/L_V ratios despite using different isochrones and stellar libraries; they all agree within $< 10\%$.

SSP models with fixed IMFs predict that M/L increases with metallicity in the V-band, as a result of line blanketing (e.g. Bruzual & Charlot 2003; Maraston 2005). However, as we have extended the range of M/L_V versus $[\text{Fe}/\text{H}]$ (Figure 10) to include two clusters — NGCs 6528 and 6553 —

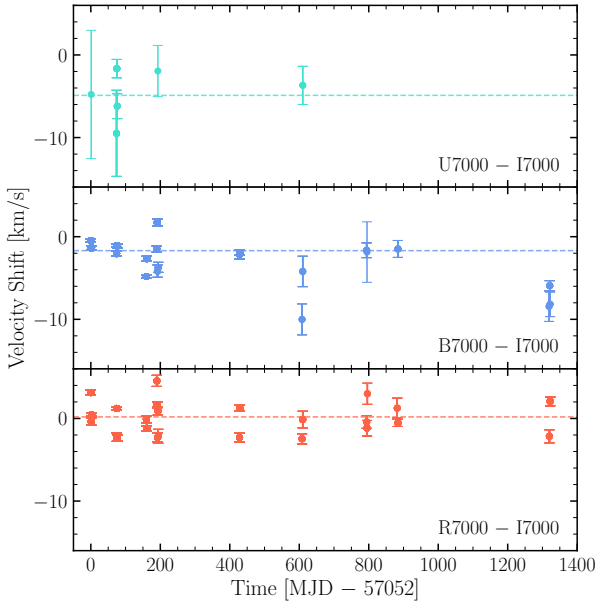


Figure 5. The average shift in velocity in the U7000 (turquoise), B7000 (blue), and R7000 (red) gratings with respect to the I7000 grating. The average velocity shift is shown as a dashed line. Shifts are calculated by taking the differences in velocity measurements that are associated with the same star, and then averaging over all the velocity differences from all stars each night.

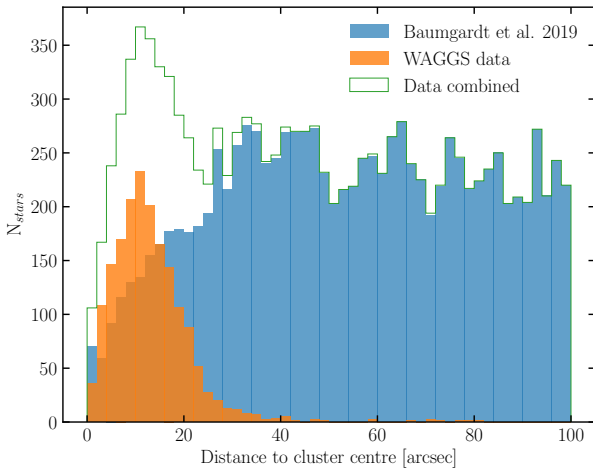


Figure 6. The number of our radial velocity measurements of the 59 Milky Way globular clusters in our sample. We apply a cut at 100 arcsec to emphasize our data at the cluster centre. In blue are the previous values already in the Baumgardt et al. (2019a) sample. In orange are the measurements that we contribute, the majority of which lie at the cluster centres (mostly within 20 arcsec), significantly increasing the number of velocity measurements in this parameter space. The green outline shows the cumulative sum of the total sample used for N -body modelling.

at higher metallicity, it is clear to see that the M/L_V ratio remains constant. The models and observations are well matched at lower metallicities, until $[\text{Fe}/\text{H}] \sim -1.0$ dex when they begin to diverge.

5.1 Comparisons to previous work

Since Strader et al. (2009, 2011) first showed the discrepancy between the M/L ratios of stellar population models and globular clusters within M31, several other studies have focused their attention on Galactic GCs (Kimmig et al. 2015; Watkins et al. 2015; Baumgardt 2017; Voggel et al. 2019).

Kimmig et al. (2015) studied the M/L of 25 Galactic GCs, with metallicities going up to -0.46 dex. They compared their observations to SSP models at an age of 13 Gyr (Mieske et al. 2013), and found no evidence for an increase in M/L with metallicity. Watkins et al. (2015) used *HST* proper motions of Bellini et al. (2014) to determine dynamical M/L ratios of 15 MW clusters up to ~ -0.5 dex. They observed the same decrease in M/L as Strader et al. (2011) towards the metal-rich end. When compared to the M/L population-synthesis estimates of McLaughlin & van der Marel (2005), the metal-poor clusters agree, but offsets exist for the clusters above $[\text{Fe}/\text{H}] = -1.0$ dex. The work of Baumgardt (2017) included five GCs with $-1.0 < [\text{Fe}/\text{H}] < -0.3$ dex, but due to large uncertainties they are uncertain if the SSP models are in fact very different to the observations at higher metallicities. Finally, Voggel et al. (2019) studied the M/L of Ultra Compact Dwarfs (UCDs). The authors showed that four UCDs — which have roughly solar metallicity — also lie at a M/L below the theoretical prediction, after accounting for the impact of their supermassive black holes.

We find that our results remain consistent with previous work and add further evidence to the discrepancy between stellar population models and observations. The SSP models that we use are typical of those used in previous literature. However, it is well known that other factors like age or the fraction of compact remnants will have an effect on the M/L of a cluster. We now explore these effects in more detail, in reference to Galactic GCs.

5.2 Cluster ages

Older clusters have a larger fraction of evolved stars compared to younger clusters, increasing the light emitted by a GC, and thus lowering M/L . Since the most metal-rich GCs in the MW are ~ 2.5 Gyr younger than the most metal-poor GCs (e.g. VandenBerg et al. 2013), we expect that M/L will decrease at higher metallicity. Haghi et al. (2017) examined an empirical relation between age and metallicity and the effect on M/L for M31 GCs but required the most metal-rich GCs in M31 to have significantly younger ages than is observed (e.g. Caldwell et al. 2011).

We follow a different approach, taking the age-metallicity relation derived by Kruijssen et al. (2019) to predict the age of each GC based on its metallicity, and then interpolate to determine the empirical M/L ratio (Figure 10; orange line). This decreases the M/L ratio as expected, particularly from $[\text{Fe}/\text{H}] = -1.0$ dex and above, but not enough to account for the difference between the models and observations at the metal-rich end i.e. the influence of age is minimal. We find that the GCs would need to be as young as ~ 6 Gyr in order for the models to agree, similar to what Voggel et al. (2019) find for UCDs, but this is several Gyr younger than the ages measured for metal-rich Galactic GCs (e.g. VandenBerg et al. 2013). As more observations of younger LMC and SMC clusters become available, it will be possible

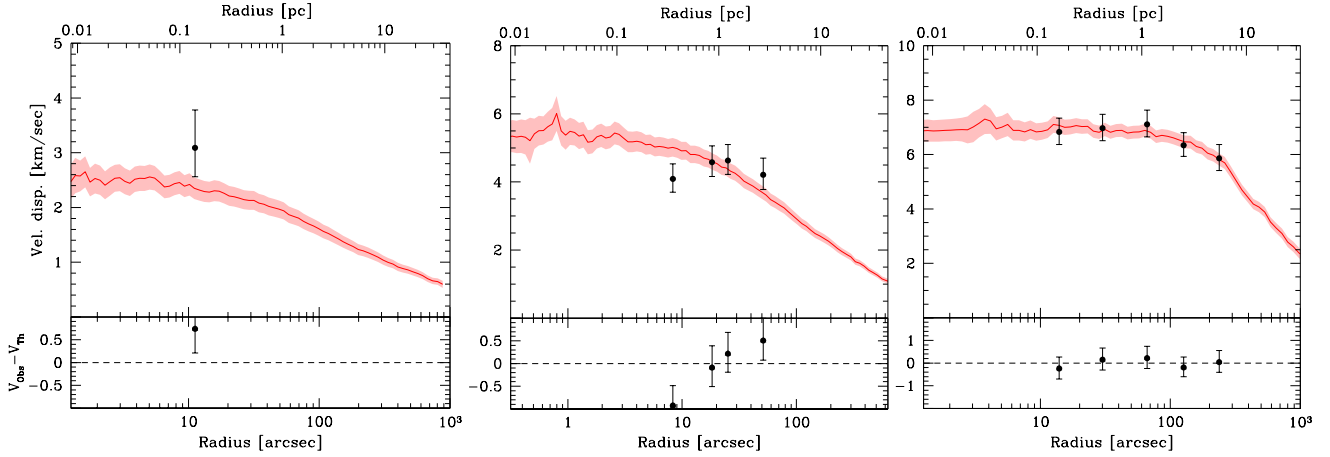


Figure 7. *N*-body fits for NGC 6717 (left), NGC 6528 (middle), and NGC 6553 (right) radial velocities (not including proper motions). The reduced chi-squared values are 3.60, 1.60, and 0.14, respectively.

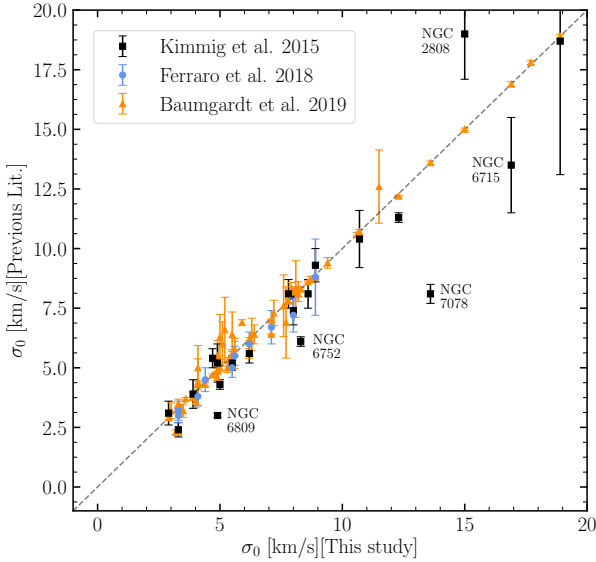


Figure 8. The (1D) central velocity dispersions of 59 WAGGS Milky Way globular clusters compared to Kimmig et al. (2015, black squares), Ferraro et al. (2018, blue circles), and Baumgardt et al. (2019a, orange triangles). Some of the most discrepant GCs from Kimmig et al. (2015) are labelled.

to see how their M/L relates to older MW GCs, which may shed more light on the effect of cluster age.

5.3 Mass function variations

The M/L ratio of a stellar population strongly depends on its present day mass function (PDMF). Dynamical evolution or a varying IMF could alter the proportions of high- or low-mass stars present within a cluster, therefore changing the PDMF in comparison to a Kroupa IMF.

Strader et al. (2009, 2011) argued that the M/L -[Fe/H] relation cannot be due to dynamical effects since the metal-rich and metal-poor GCs of M31 are of similar mass and size. Instead they proposed different IMFs for the metal-rich and metal-poor clusters to try and explain the discrepancy.

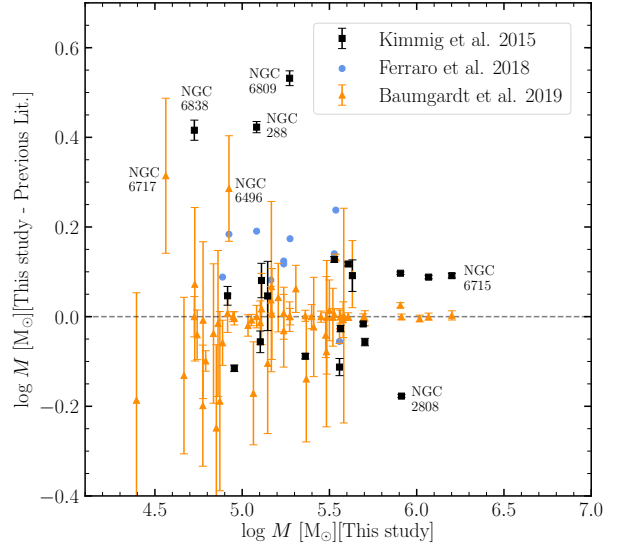


Figure 9. The masses of Milky Way globular clusters derived here compared to Kimmig et al. (2015); Ferraro et al. (2018); Baumgardt et al. (2019a), the same as in Figure 8. Some of the most discrepant Kimmig et al. (2015); Baumgardt et al. (2019a) GCs are labelled.

Zonoozi et al. (2016) looked at the effects of a varying IMF for M31 GCs in more detail. They found that a top-heavy IMF, in combination with other effects e.g. dynamical evolution and remnant retention (see Section 5.4 for more detail) improved the agreement between SSP models and M/L observations.

Here we explore the effect of introducing a bottom-light mass function on the SSP models. Using the MIST isochrones, C3K spectral library (Conroy et al. in prep), and their synthetic V -band photometry, we calculate models with three different PDMF (Figure 11; solid lines):

- (i) Kroupa IMF, $\alpha = -1.3$ ($M < 0.5 M_{\odot}$), $\alpha = -2.3$ ($M > 0.5 M_{\odot}$) [yellow];

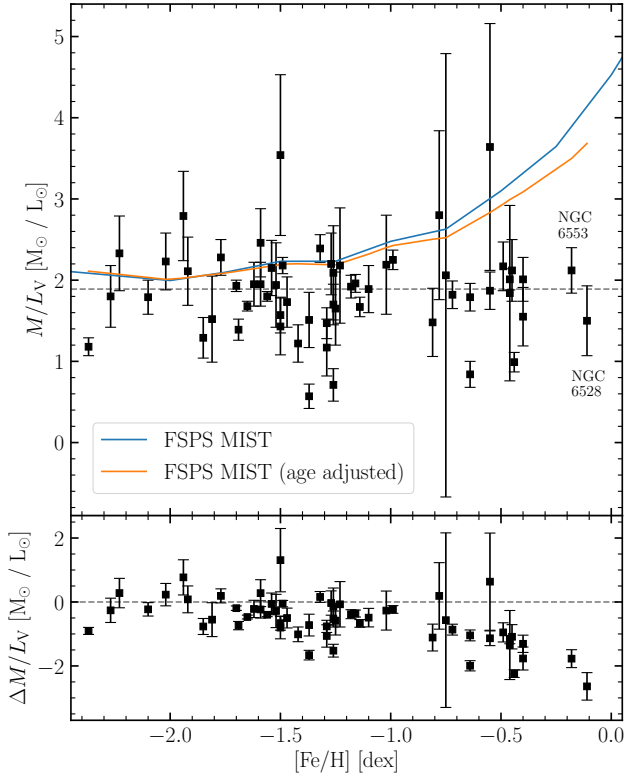


Figure 10. The mass-to-light ratio of Milky Way globular clusters versus metallicity. Over-plotted are the original FSPS MIST model at 12.59 Gyr (blue) and a 2D interpolated version which accounts for the age-metallicity relation derived by [Kruijssen et al. \(2019\)](#) (orange). The median M/L ratio is shown as a grey dashed line. The difference in M/L between each GC and the original FSPS MIST model is shown underneath.

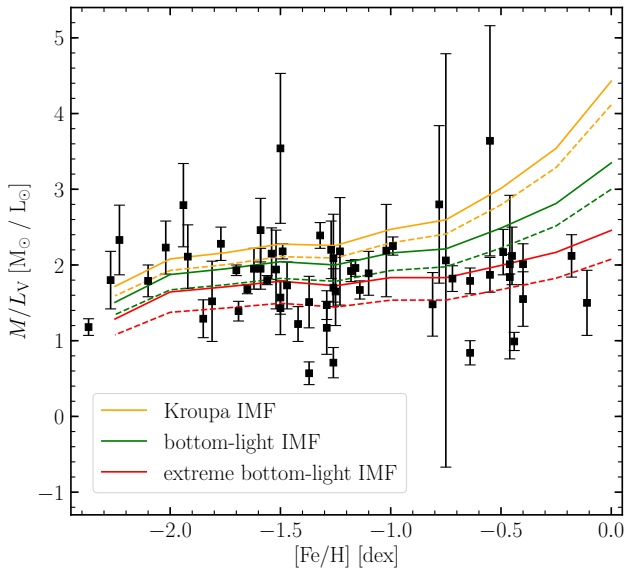


Figure 11. M/L of Milky Way globular clusters versus $[\text{Fe}/\text{H}]$ for a Kroupa IMF (yellow), bottom-light mass function (green), and an extreme bottom-light mass function (red). The solid lines represent 100% retention of remnants (i.e. NSs and BHs), compared to 0% remnant retention (dashed lines).

(ii) bottom-light mass function, $\alpha = -1.3$ ($M < 1.0 M_\odot$), $\alpha = -2.3$ ($M > 1.0 M_\odot$) [green];

(iii) extreme bottom-light mass function, $\alpha = -0.3$, ($M < 1.0 M_\odot$), $\alpha = -2.3$ ($M > 1.0 M_\odot$) [red].

For all models we integrate the mass function between 0.08 and $100 M_\odot$ and use the same prescription for remnant masses as used by [Renzini & Ciotti \(1993\)](#).

Only the M/L of the third model are low enough to replicate the observations above -1.0 dex, however, there is strong evidence that it is nonphysical for the IMF to vary so strongly with $[\text{Fe}/\text{H}]$ ([Bastian et al. 2010](#)). A more detailed study of the influence of the mass function is left for future work. Next, we look to the retention of remnants as another possible effect on the M/L .

5.4 Remnant retention

As stars evolve into remnants, M/L increases — stellar remnants continue contributing to the mass but no longer to the luminosity of a globular cluster. The strength of this effect depends on the number of remnants that are retained throughout a cluster’s lifetime. It is expected that at least some proportion of compact remnants (black holes and neutron stars) will either receive a velocity kick when they form and become immediately ejected, or will eventually be expelled from the cluster as a result of dynamical evolution (e.g. [Weatherford et al. 2018](#); [Kremer et al. 2019](#), and references therein). These compact remnants are removed in conjunction with the evaporation of low-mass stars, a result of mass segregation.

Previous work has shown that a spread in the retention fraction of compact remnants — along with metallicity-dependent mass segregation effects — can explain the M/L - $[\text{Fe}/\text{H}]$ discrepancy of MW clusters ([Shanahan & Gieles 2015](#)). Other work has found that by reducing the remnant retention fraction to 30% (along with a top-heavy IMF), the discrepancy between the models and observations decreased ([Zonoozi et al. 2016](#)). The latter study explored this further by introducing a dependence on cluster mass and metallicity, which improved their SSP predictions for M31 GCs.

We explore the effect of removing remnants upon the SSP models, by adapting the models from Section 5.3 which follow 100% black hole (BH) and neutron star (NS) retention. We calculate the equivalent models for the most extreme case: 0% BH+NS retention in the range $-2.25 < [\text{Fe}/\text{H}] < 0.00$ for each mass function, at an age of 12.59 Gyr (Figure 11; dashed lines). As expected, this has the effect of decreasing M/L_V for all metallicities. At $[\text{Fe}/\text{H}] = 0$ dex, the effect of removing all BHs and NSs is $\sim 7\%$ for a Kroupa IMF [case (i)] or $\sim 20\%$ for the bottom-light mass functions [cases (ii) and (iii)].

While a 0% BH+NS retention fraction alone is not enough to explain the discrepancy, we clearly observe some effect. In order to better approximate the percentage of remnants retained within a cluster, it is crucial for future studies to determine the remnant fraction, particularly at the metal-rich end.

5.5 Other possible effects

As we have shown in the previous sections, accounting for the younger ages of an increasingly metal-rich cluster population and testing for the effect of removing remnants both serve to decrease M/L . Yet each effect alone is not enough to explain the discrepancy between the observed and theoretically predicted M/L . Therefore, a combination of the explored effects, or some other effects must be at play.

It is already known that a strong correlation is observed between the dynamical age of a globular cluster and the low-mass slope of its mass function (e.g. [Sollima & Baumgardt 2017](#)). In other words, mass segregation leads to a preferential loss of low-mass stars in the Galactic tidal fields, impacting on the evolution of a cluster. Therefore, since metal-rich MW clusters are only found in the bulge where they are subject to significant dynamical effects, we expect that they will lose a larger fraction of low-mass stars and have a lower M/L . Our N -body models take tidal fields into account by adjusting the initial mass function; we note that this approach may be limited in its accuracy.

[Shanahan & Gieles \(2015\)](#) found that mass segregation leads to a bias in the determination of M/L , which was not taken into account by the models of [Strader et al. \(2011\)](#). This bias is accounted for by our N -body models, however, so it is unlikely that this could explain the discrepancy between the observed M/L ratio and SSP models. This effect may also explain why [Strader et al. \(2011\)](#) find a decrease in M/L with metallicity, while we see a flat relation.

The dynamical evolution of a cluster also depends on its radius; GCs with small radii evolve more quickly. This is true both for Milky Way clusters and their extragalactic counterparts (see [Usher et al. 2013](#) and references therein). Since metal-rich GCs have smaller radii on average — smaller galactocentric radii leads to stronger tidal fields — metal-rich GCs should lose more low-mass stars, i.e. they will have a more bottom-light mass function compared to metal-poor GCs with the same mass. Thus we would expect metal-rich GCs to have lower M/L compared to the predictions of a stellar population calculated using the IMF alone.

The internal configuration of a cluster itself is also of primary importance (e.g. density, initial tidal filling configuration, relaxation time). More compact clusters evolve faster dynamically, decreasing their M/L accordingly. [Bianchini et al. \(2017\)](#) suggest that possible differences in internal configurations between metal-rich and metal-poor clusters (e.g. metal-rich clusters being more dense) could produce a different dynamical evolution of the M/L , therefore decreasing the M/L of metal-rich clusters. This effect could add up to the evolution due to the tidal field.

Another possible cause could lie with the shortcomings of the N -body models e.g. binaries or rotation. However, we expect binaries and rotation to be more effectively destroyed in metal-rich clusters, since the inner metal-rich GCs are more compact. In future work, it would be interesting to make a more detailed comparison between clusters in the bulge and in the halo, as a more robust test for dynamical effects upon GCs.

Finally, we rule out dark matter as a possible effect, as there is no evidence for dark matter in any MW globular cluster thus far ([Sollima et al. 2009](#); [Ibata et al. 2011](#)).

6 SUMMARY

In this work, we have determined 1,622 radial velocity measurements across 59 Milky Way clusters. The majority of the stars are located in the centres of GCs (within 20 arcsec), extending prior work to a new region of parameter space. Incorporating this new data, we recalculate dynamical parameters (i.e. central velocity dispersions and masses). Importantly, two new MW clusters with $[\text{Fe}/\text{H}] \gtrsim -0.4$ dex have been introduced — where previous data had been lacking — allowing us to better understand the M/L_V - $[\text{Fe}/\text{H}]$ relation at the metal-rich end.

Our results confirm previous work by [Baumgardt \(2017\)](#); the mass-to-light ratio of GCs does not change with metallicity for Milky Way clusters. Subsequently, we now see an even greater divergence with SSP models, strengthening the concern that we need to decipher where this discrepancy originates. Having looked at possible explanations, it seems reasonable to assume that dynamical effects have a significant part to play in the solution. Moreover, globular clusters undergo internal dynamical evolution much more rapidly than galaxies, and is further accelerated for the metal-rich clusters located in the bulge. This suggests that it is not straightforward to compare globular clusters with galaxies, particularly towards higher metallicities. Either more equivalent calibrators need to be found, or we need to improve our understanding of the dynamical processes so that they can be accounted for in the models. Further work in this area has the potential to reveal a new understanding of the dynamics of globular clusters.

ACKNOWLEDGEMENTS

We thank the anonymous referee for their helpful and insightful comments. Nate Bastian, Christopher Usher, and Sebastian Kamann gratefully acknowledge support from the European Research Council (ERC-CoG-646928, Multi-Pop). Nate Bastian also gratefully acknowledges financial support from the Royal Society (University Research Fellowship), and Pierluigi Cerulo acknowledges the support of a ALMA-CONICYT grant no. 31180051.

Additionally, we acknowledge the use of archival observations made with the NASA/ESA Hubble Space Telescope, obtained at the Space Telescope Science Institute, which is operated by AURA, Inc., under NASA contract NAS 5-26555. We also used data from the European Space Agency (ESA) mission *Gaia* (<https://www.cosmos.esa.int/gaia>), processed by the *Gaia* Data Processing and Analysis Consortium (DPAC, <https://www.cosmos.esa.int/web/gaia/dpac/consortium>). Funding for the DPAC has been provided by national institutions, in particular the institutions participating in the *Gaia* Multilateral Agreement.

Finally, we note that this work made use of NUMPY ([van der Walt et al. 2011](#)), SCIPY ([Jones et al. 2001](#)), MATPLOTLIB ([Hunter 2007](#)), ASTROPY ([Astropy Collaboration et al. 2013](#)), and PYRAF, a product of the Space Telescope Science Institute.

REFERENCES

Anderson J., Bedin L. R., 2010, *PASP*, **122**, 1035

- Anderson J., Ryon J. E., 2018, Technical report, Improving the Pixel-Based CTE-correction Model for ACS/WFC
- Ashman K. M., Zepf S. E., 1998, *Globular Cluster Systems*
- Astropy Collaboration et al., 2013, *A&A*, **558**, A33
- Bastian N., Covey K. R., Meyer M. R., 2010, *ARA&A*, **48**, 339
- Baumgardt H., 2017, *MNRAS*, **464**, 2174
- Baumgardt H., Hilker M., 2018, *MNRAS*, **478**, 1520
- Baumgardt H., Hilker M., Sollima A., Bellini A., 2019a, *MNRAS*, **482**, 5138
- Baumgardt H., et al., 2019b, *MNRAS*, **488**, 5340
- Bellini A., Anderson J., Bedin L. R., 2011, *PASP*, **123**, 622
- Bellini A., et al., 2014, *ApJ*, **797**, 115
- Bellini A., Anderson J., Bedin L. R., King I. R., van der Marel R. P., Piotto G., Cool A., 2017a, *ApJ*, **842**, 6
- Bellini A., Bianchini P., Varri A. L., Anderson J., Piotto G., van der Marel R. P., Vesperini E., Watkins L. L., 2017b, *ApJ*, **844**, 167
- Bellini A., Anderson J., Grogan N. A., 2018a, Technical report, Focus-diverse, empirical PSF models for the ACS/WFC
- Bellini A., et al., 2018b, *ApJ*, **853**, 86
- Bianchini P., Sills A., van de Ven G., Sippel A. C., 2017, *MNRAS*, **469**, 4359
- Bruzual G., Charlot S., 2003, *MNRAS*, **344**, 1000
- Caldwell N., Schiavon R., Morrison H., Rose J. A., Harding P., 2011, *AJ*, **141**, 61
- Cappellari M., et al., 2012, *Nature*, **484**, 485
- Carretta E., Bragaglia A., Gratton R. G., Recio-Blanco A., Lucatello S., D'Orazi V., Cassisi S., 2010, *A&A*, **516**, A55
- Childress M., Vogt F., Nielsen J., Sharp R., 2014a, PyWiFeS: Wide Field Spectrograph data reduction pipeline, Astrophysics Source Code Library (ascl:1402.034)
- Childress M. J., Vogt F. P. A., Nielsen J., Sharp R. G., 2014b, *Ap&SS*, **349**, 617
- Choi J., Dotter A., Conroy C., Cantiello M., Paxton B., Johnson B. D., 2016, *ApJ*, **823**, 102
- Conroy C., 2013, *Annual Review of Astronomy and Astrophysics*, **51**, 393
- Conroy C., Gunn J. E., 2010, *ApJ*, **712**, 833
- Conroy C., Gunn J. E., White M., 2009, *ApJ*, **699**, 486
- Dallessandro E., Schiavon R. P., Rood R. T., Ferraro F. R., Sohn S. T., Lanzoni B., O'Connell R. W., 2012, *AJ*, **144**, 126
- Dallessandro E., et al., 2014, *ApJ*, **791**, L4
- Dias B., Barbay B., Saviane I., Held E. V., Da Costa G. S., Ortolani S., Gullieuszik M., Vásquez S., 2016, *A&A*, **590**, A9
- Djorgovski S. G., Gal R. R., McCarthy J. K., Cohen J. G., de Carvalho R. R., Meylan G., Bendinelli O., Parmeggiani G., 1997, *ApJ*, **474**, L19
- Dopita M., Hart J., McGregor P., Oates P., Bloxham G., Jones D., 2007, *Ap&SS*, **310**, 255
- Dopita M., et al., 2010, *Ap&SS*, **327**, 245
- Dotter A., 2016, *ApJS*, **222**, 8
- Dotter A., Sarajedini A., Anderson J., 2011, *ApJ*, **738**, 74
- Ferraro F. R., et al., 2018, *ApJ*, **860**, 50
- Gaia Collaboration et al., 2016, *A&A*, **595**, A1
- Gaia Collaboration et al., 2018, *A&A*, **616**, A1
- Gallazzi A., Bell E. F., 2009, *ApJS*, **185**, 253
- Gieles M., Zocchi A., 2015, *MNRAS*, **454**, 576
- Giesers B., et al., 2018, *MNRAS*, **475**, L15
- Giesers B., et al., 2019, *A&A*, **632**, A3
- Gilliland R. L., Rajan A., Deustua S., 2010, Technical report, WFC3 UVIS Full Well Depths, and Linearity Near and Beyond Saturation
- Girardi L., Bressan A., Bertelli G., Chiosi C., 2000, *A&AS*, **141**, 371
- Greenfield P., White R. L., 2000, in Manset N., Veillet C., Crabtree D., eds, *Astronomical Society of the Pacific Conference Series Vol. 216, Astronomical Data Analysis Software and Systems IX*. p. 59
- Greenfield P., White R. L., 2006, in Koekemoer A. M., Goudfrooij P., Dressel L. L., eds, *The 2005 HST Calibration Workshop: Hubble After the Transition to Two-Gyro Mode*. p. 437
- Gunn J. E., Griffin R. F., 1979, *AJ*, **84**, 752
- Haghi H., Khalaj P., Hasani Zonoozi A., Kroupa P., 2017, *ApJ*, **839**, 60
- Harris W. E., 1996, *AJ*, **112**, 1487
- Harris W. E., 2010, arXiv e-prints, p. arXiv:1012.3224
- Heggie D. C., 2014, *MNRAS*, **445**, 3435
- Hunter J. D., 2007, *Computing In Science & Engineering*, **9**, 90
- Husser T.-O., Wende-von Berg S., Dreizler S., Homeier D., Reinerters A., Barman T., Hauschildt P. H., 2013, *A&A*, **553**, A6
- Ibata R., Sollima A., Nipoti C., Bellazzini M., Chapman S. C., Dallessandro E., 2011, *ApJ*, **738**, 186
- Jones E., Oliphant T., Peterson P., 2001, SciPy: Open source scientific tools for Python, <http://www.scipy.org/>
- Kamann S., Wisotzki L., Roth M. M., 2013, *A&A*, **549**, A71
- Kamann S., Wisotzki L., Roth M. M., Gerssen J., Husser T. O., Sandin C., Weilbacher P., 2014, *A&A*, **566**, A58
- Kamann S., et al., 2018, *MNRAS*, **473**, 5591
- Kimmig B., Seth A., Ivans I. I., Strader J., Caldwell N., Anderton T., Gregersen D., 2015, *AJ*, **149**, 53
- King I., 1962, *AJ*, **67**, 471
- King I. R., 1966, *AJ*, **71**, 64
- Kremer K., Lu W., Rodriguez C. L., Lachat M., Rasio F. A., 2019, *ApJ*, **881**, 75
- Kroupa P., 2001, *MNRAS*, **322**, 231
- Kruijssen J. M. D., Pfeffer J. L., Reina-Campos M., Crain R. A., Bastian N., 2019, *MNRAS*, **486**, 3180
- Maraston C., 2005, *MNRAS*, **362**, 799
- Martins L. P., Lima-Dias C., Coelho P. R. T., Laganá T. F., 2019, *MNRAS*, **484**, 2388
- McLaughlin D. E., van der Marel R. P., 2005, *The Astrophysical Journal Supplement Series*, **161**, 304
- Mieske S., Frank M. J., Baumgardt H., Lützgendorf N., Neumayer N., Hilker M., 2013, *A&A*, **558**, A14
- Newman A. B., Treu T., Ellis R. S., Sand D. J., 2013, *ApJ*, **765**, 25
- Nitadori K., Aarseth S. J., 2012, *MNRAS*, **424**, 545
- Paxton B., Bildsten L., Dotter A., Herwig F., Lesaffre P., Timmes F., 2011, *ApJS*, **192**, 3
- Paxton B., et al., 2013, *ApJS*, **208**, 4
- Paxton B., et al., 2015, *ApJS*, **220**, 15
- Pietrinferni A., Cassisi S., Salaris M., Castelli F., 2004, *ApJ*, **612**, 168
- Piotto G., et al., 2002, *A&A*, **391**, 945
- Pryor C., Meylan G., 1993, in Djorgovski S. G., Meylan G., eds, *Astronomical Society of the Pacific Conference Series Vol. 50, Structure and Dynamics of Globular Clusters*. p. 357
- Renzini A., Ciotti L., 1993, *ApJ*, **416**, L49
- Sánchez-Blázquez P., et al., 2006, *MNRAS*, **371**, 703
- Science Software Branch at STScI 2012, PyRAF: Python alternative for IRAF, Astrophysics Source Code Library (ascl:1207.011)
- Shanahan R. L., Gieles M., 2015, *MNRAS*, **448**, L94
- Sirianni M., et al., 2005, *PASP*, **117**, 1049
- Sollima A., Baumgardt H., 2017, *MNRAS*, **471**, 3668
- Sollima A., Bellazzini M., Smart R. L., Correnti M., Pancino E., Ferraro F. R., Romano D., 2009, *MNRAS*, **396**, 2183
- Soto M., et al., 2017, *AJ*, **153**, 19
- Stetson P. B., 1984, *PASP*, **96**, 128
- Stetson P. B., 1987, *PASP*, **99**, 191
- Strader J., Smith G. H., Larsen S., Brodie J. P., Huchra J. P., 2009, *AJ*, **138**, 547
- Strader J., Caldwell N., Seth A. C., 2011, *AJ*, **142**, 8
- Tonry J., Davis M., 1979, *AJ*, **84**, 1511
- Torniamanti S., Bertin G., Bianchini P., 2019, arXiv e-prints, p. arXiv:1909.13093

- Usher C., Forbes D. A., Spitler L. R., Brodie J. P., Romanowsky A. J., Strader J., Woodley K. A., 2013, *MNRAS*, **436**, 1172
- Usher C., et al., 2017, *MNRAS*, **468**, 3828
- Usher C., et al., 2019, *MNRAS*, **482**, 1275
- VandenBerg D. A., Brogaard K., Leaman R., Casagrande L., 2013, *ApJ*, **775**, 134
- Vazdekis A., Koleva M., Ricciardelli E., Röck B., Falcón-Barroso J., 2016, *MNRAS*, **463**, 3409
- Voggel K. T., Seth A. C., Baumgardt H., Mieske S., Pfeffer J., Raskazov A., 2019, *ApJ*, **871**, 159
- Wang L., et al., 2016, *MNRAS*, **458**, 1450
- Watkins L. L., van der Marel R. P., Bellini A., Anderson J., 2015, *ApJ*, **812**, 149
- Weatherford N. C., Chatterjee S., Rodriguez C. L., Rasio F. A., 2018, *ApJ*, **864**, 13
- Zocchi A., Gieles M., Hénault-Brunet V., 2017, *MNRAS*, **468**, 4429
- Zonoozi A. H., Küpper A. H. W., Baumgardt H., Haghi H., Kroupa P., Hilker M., 2011, *MNRAS*, **411**, 1989
- Zonoozi A. H., Haghi H., Kroupa P., 2016, *ApJ*, **826**, 89
- de La Peña M. D., White R. L., Greenfield P., 2001, in Harnden Jr. F. R., Primini F. A., Payne H. E., eds, *Astronomical Society of the Pacific Conference Series Vol. 238, Astronomical Data Analysis Software and Systems X*. p. 59
- di Nino D., Makidon R. B., Lallo M., Sahu K. C., Sirianni M., Casertano S., 2008, Technical report, HST Focus Variations with Temperature
- van Dokkum P. G., 2001, *PASP*, **113**, 1420
- van der Walt S., Colbert S. C., Varoquaux G., 2011, *Computing in Science Engineering*, **13**, 22

This paper has been typeset from a $\text{\TeX}/\text{\LaTeX}$ file prepared by the author.